Enhanced Atom Interferometer Readout through the Application of Phase Shear

Alex Sugarbaker, Susannah M. Dickerson, Jason M. Hogan, David M. S. Johnson, and Mark A. Kasevich*

Department of Physics, Stanford University, Stanford, California 94305, USA

(Received 14 May 2013; published 10 September 2013)

We present a method for determining the phase and contrast of a single shot of an atom interferometer. The application of a phase shear across the atom ensemble yields a spatially varying fringe pattern at each output port, which can be imaged directly. This method is broadly relevant to atom-interferometric precision measurement, as we demonstrate in a 10 m ^{87}Rb atomic fountain by implementing an atom-interferometric gyrocompass with 10 mdeg precision.

DOI: 10.1103/PhysRevLett.111.113002 PACS numbers: 37.25.+k, 03.75.Dg, 06.30.Gv

Light-pulse atom interferometers use optical pulses to split, redirect, and interfere freely falling atoms [1]. They have proven widely useful for precision metrology. Atom interferometers have measured the gravitational [2,3] and fine-structure [4] constants, are used in ongoing laboratory tests of the equivalence principal [5] and general relativity [6,7], and have been proposed for use in gravitational wave detection [8,9]. They have also enabled the realization of high performance gyroscopes [10], accelerometers [11], gravimeters [12], and gravity gradiometers [13].

Current-generation light-pulse atom interferometers determine phase shifts by recording atomic transition probabilities [1]. These are inferred from the populations of the two atomic states that comprise the interferometer output ports. Because of experimental imperfections, interference contrast is not perfect—the dark port never exhibits complete extinction. It is therefore necessary to independently characterize contrast prior to inferring phase. Typically, this is done with a sequence of multiple shots with different phases, such that the population ratio is scanned through the contrast envelope [14]. Such a protocol relies on the stability of the contrast envelope. In many cases, the contrast varies from shot to shot, introducing additional noise and bias in the phase extraction process.

We present a broadly applicable technique capable of resolving interference phase on a single experimental shot. This is accomplished by introducing a phase shear across the spatial extent of the atom ensemble. The shear is manifest in a spatial variation of the atomic transition probability, which, under appropriate conditions, can be directly observed in an image of the cloud [Fig. 1(b)]. Using this phase shear readout (PSR), it is no longer necessary to vary the phase over many shots to determine the contrast envelope. Instead, the contrast of each shot can be inferred from the depth of modulation of the spatial fringe pattern on the atom ensemble. The interferometer phase is directly determined from the phase of the spatial fringe.

PSR fringes reveal rich details about atom interferometer phase shifts and systematic effects, much as spatially varying optical interference patterns yield information about optical systems and their aberrations. The intentional application of a phase shear is analogous to the use of a wedged optical shear plate, where a large applied shear highlights small phase variations across a laser beam [15].

Previous work has employed spatial modulation of the atom population in a variety of atom interferometry experiments [16–23]. Here, we use beam pointing to introduce shear in a way that is broadly applicable to existing light-pulse interferometer configurations. In particular, this method does not require Bose-Einstein condensed or ultracold-atomic sources. Moreover, manipulating and measuring the spatial population modulation facilitates measurements of small phase gradients, as we demonstrate by implementing a precise atom-interferometric gyrocompass. Finally, we demonstrate arbitrary control over the phase shear axis by combining laser beam pointing and atom-optics pulse timing asymmetry.

The apparatus and methods are similar to our previous work [24]. Using evaporative cooling followed by a magnetic lens, we obtain a cloud of 4×10^6 ^{87}Rb atoms with a radius of 200 μm and a temperature of 50 nK [25]. These atoms are prepared in the magnetically insensitive $|F = 2, m_F = 0\rangle$ state and launched vertically into an 8.7 m vacuum tube with a chirped optical lattice. They fall back to the bottom after 2.6 s, and we use a vertical fluorescence beam to image them onto two perpendicular CCD cameras (Fig. 1).

While the atoms are in free fall in a magnetically shielded region [26], we perform light-pulse atom interferometry with a $\pi/2$-π-$\pi/2$ acceleration-sensitive configuration with a duration of $2T = 2.3$ s. The atom-optics pulses are applied along the vertical axis using two-photon Raman transitions between the $|F=2, m_F=0\rangle$ and $|F=1, m_F=0\rangle$ hyperfine ground states (the lasers are detuned 1.0 GHz blue of the $|F = 2\rangle \rightarrow |F' = 3\rangle$ transition of the D_2 line). The atom-optics light is delivered from above and retroreflected off of an in-vacuum piezoactuated tip-tilt mirror.

The effective wave vector $\mathbf{k}_{\text{eff}}$ of the Raman transitions is determined by the pointing direction of the retroreflection mirror [5], which is set for each atom-optics pulse with 1 nrad precision. The mirror has three independent piezoactuators in a tripod configuration that allow arbitrary

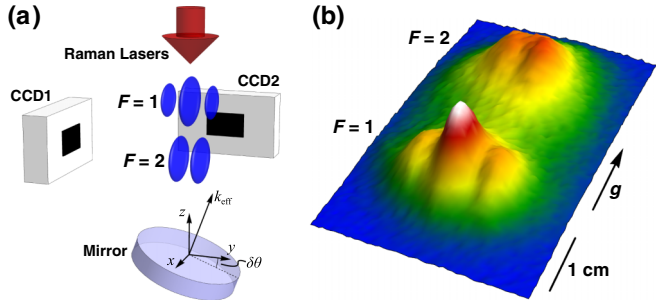

FIG. 1 (color online). (a) Schematic diagram of the apparatus, showing beam-tilt phase shear readout. Atoms are cooled and launched upward into an interferometer region, which is not shown. Once they fall back to the bottom, the wave packets are overlapped, yielding an interference pattern (blue fringes) imaged by two perpendicular cameras (CCD1,2). An additional optical pulse separates the output ports ($F = 1$ and $F = 2$) by pushing the $F = 2$ atoms downward. All atom-optics pulses are performed by lasers incident from above and retroreflected off of a piezoactuated mirror. Tilting this mirror by an angle $\delta\theta$ for the third atom-optics pulse yields a phase shear. (b) A fluorescence image of the atomic density distribution taken with CCD2 after interference. Spatial fringes result from a third-pulse tilt $\delta\theta = 60$ μrad about the x axis. The pushed $F = 2$ atoms are heated, yielding reduced apparent contrast, and we ignore the $F = 2$ port in subsequent analysis.

two-axis tip-tilt control. We compensate for phase shifts arising from Earth's rotation by applying appropriate tilts for each of the three pulses [5,24], but additional mirror tilts can be used to induce shear for PSR.

To generate a controlled phase shear, we tilt the piezoactuated mirror for the final $\pi/2$ pulse by an angle $\delta\theta$ with respect to the initial two pulses (in addition to the tilts needed for rotation compensation). In the semiclassical limit, the phase shift for a three-pulse interferometer is $\Delta\Phi = \mathbf{k}_1 \cdot \mathbf{x}_1 - 2\mathbf{k}_2 \cdot \mathbf{x}_2 + \mathbf{k}_3 \cdot \mathbf{x}_3$, where $\mathbf{k}_i \equiv \mathbf{k}_{\mathrm{eff},i}$ is the effective propagation vector at the time of the ith pulse and $\mathbf{x}_i$ is the classical position of the atom [1,14]. For example, tilting $\mathbf{k}_3$ by an additional angle $\delta\theta$ about the x axis yields a phase $\Phi_H = k_{\mathrm{eff}}\delta\theta y_3$ across the cloud, where y_3 is the horizontal position at the third pulse [Fig. 1(a)]. This shear is independent of the details of the previous atom-laser interactions and of the implementation of the atomic source (in particular, its spatial extent, temperature, and quantum degeneracy).

Figure 1(b) shows an image of the interferometer output with horizontal phase shear. An optical "pushing" pulse, 5 μs long and resonant with the $|F = 2\rangle \rightarrow |F' = 3\rangle$ transition, spatially separates the interferometer output ports [27]. Complementary fringes appear across each port, corresponding to the spatial variation of the atomic transition probability. For linear shears, we can write the phase as $\phi(\mathbf{r}) = \boldsymbol{\kappa} \cdot \mathbf{r} + \phi_0$, where ϕ_0 is the overall interferometer phase and $\boldsymbol{\kappa}$ is the wave vector of the spatially varying component. This implies a spatial modulation of the atomic distribution given by $P(\mathbf{r}) = \frac{1}{2} + \frac{C}{2}\sin(\boldsymbol{\kappa}\cdot\mathbf{r} + \phi_0)$, where C is the contrast.

Since the retroreflection mirror can be tilted about an arbitrary horizontal axis, beam-tilt PSR can yield fringe patterns with $\hat{\boldsymbol{\kappa}}$ anywhere in the xy plane, orthogonal to the laser beam axis [see Fig. 1(a)]. For instance, it is possible to choose a tilt axis parallel to the line of sight of either CCD. We then see a spatial fringe pattern with one camera, but no contrast with the other. Hereafter, we tilt about the x axis, yielding fringes on CCD2.

The spatial frequency κ of beam-tilt PSR fringes is set by the tilt angle $\delta\theta$. Figure 2(b) shows the expected linear dependence. By appropriate choice of $\delta\theta$, the fringe period can be tuned to an arbitrary value (in practice, high spatial frequencies are limited by the depth of focus of the imaging system). Because we detect the atoms at a final drift time $t_d = 2.7$ s that is later than the third pulse time $t_3 = 2.5$ s (both measured from the time of trap release), we must correct for the continued motion of the atoms. In the limit where the initial size of the atomic source is much less than the final spatial extent of the cloud (point source limit [24,28]), the position at t_d of an atom with velocity v_y is $y \approx v_y t_d \approx y_3 t_d/t_3$. The detected horizontal fringe spatial frequency is then $\kappa_H \equiv \partial_y \Phi_H = k_{\mathrm{eff}}\delta\theta t_3/t_d$.

We demonstrate single-shot phase readout by implementing a short interferometer sequence ($2T = 50$ ms) near the end of the 2.7 s drift time. In this case, the atom cloud has a large spatial extent for the entire pulse

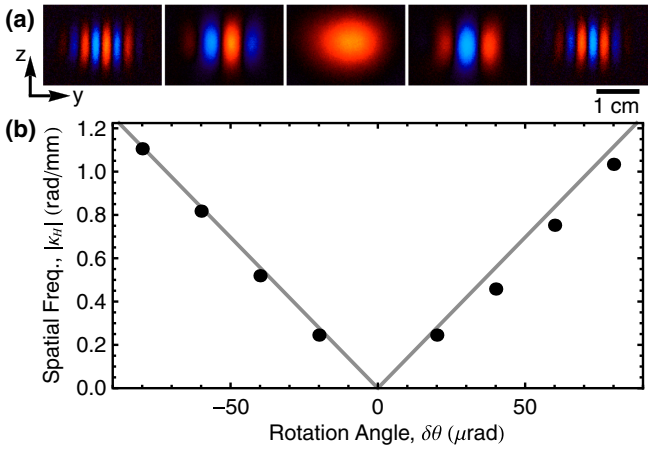

FIG. 2 (color online). Horizontal fringes resulting from beam-tilt PSR in a $2T = 2.3$ s interferometer. (a) Spatial fringes observed on CCD2 with third-pulse tilt angles $\delta\theta = -80$, -40, 0, $+40$, $+80$ μrad (left to right). Red versus blue regions show anticorrelation in atom population. Each image is the second-highest variance principal component arising from a set of 20 fluorescence images [24]. (b) Measured fringe spatial frequency $|\kappa_H|$, resulting from images filtered using principal component analysis [24,30]. We bin the images vertically and fit a Gaussian modulated by the interference term $P(\mathbf{r})$. The curve is a prediction with no free parameters that includes a reduction in the measured wavelength from heating during imaging [31].

sequence. For each shot, we set the interferometer phase with an acousto-optic modulator and read it back using beam-tilt PSR with $\delta\theta = 60\ \mu$rad. Figure 3 shows the expected correspondence between the applied and measured phases. The spread in the measured phase is due to technical noise associated with spurious vibrations of the Raman laser beam delivery optics. This spread exceeds 2π at longer interrogation times, but fringe fits still yield a precise phase for each shot.

To show how PSR can enable precision measurements, we implement an atom-interferometric gyrocompass in a long interrogation time ($2T = 2.3$ s) configuration. In this case, the Raman laser axis is rotated to compensate Earth's rotation, keeping this axis inertially fixed throughout the interrogation sequence. At the latitude of our lab in Stanford, California, this corresponds to an effective rotation rate of $\Omega_E = 57.9\ \mu$rad/s about an axis along the local true north vector, which is at an angle $\phi_E \approx 15°$ with respect to the negative x axis (coarsely determined cartographically). However, a small misalignment $\delta\phi_E \ll 1$ between the rotation axis of the retroreflection mirror and true north results in a residual rotation $\mathbf{\delta\Omega} \approx \delta\phi_E\Omega_E(\hat{\mathbf{x}}\sin\phi_E - \hat{\mathbf{y}}\cos\phi_E)$ that leads to a Coriolis phase shift $\Phi_C = 2\mathbf{k}_{\text{eff}} \cdot (\mathbf{\delta\Omega} \times \mathbf{v})T^2$ that varies across the cloud. As before, in the point source limit $v_y \approx y/t_d$, so the Coriolis phase gradient is $\kappa_{C,y} \equiv \partial_y\Phi_C = 2k_{\text{eff}}T^2\delta\phi_E\Omega_E\sin\phi_E/t_d$. To realize a gyrocompass, we vary the axis of applied rotation by scanning $\delta\phi_E$ and identify true north with the angle at which $\kappa_{C,y} = 0$.

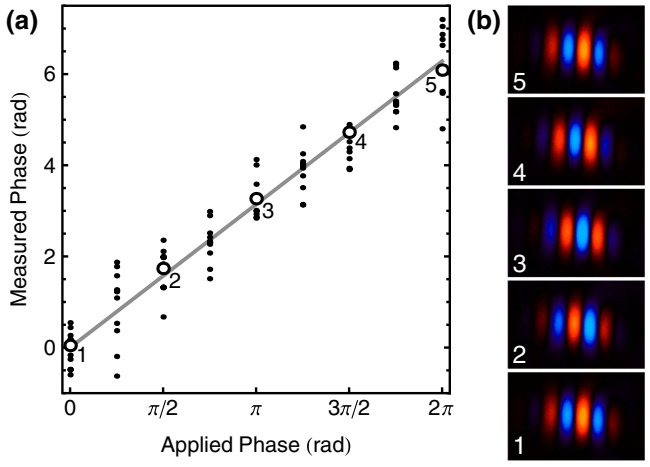

FIG. 3 (color online). Single-shot phase readout with a $2T = 50$ ms interferometer. (a) Measured phase versus the applied phase of the final atom-optics pulse for 96 shots. A line with unity slope is shown for reference. The measured phase is fit from images like those in (b). The measurement scatter is dominated by vibrations of the Raman laser beam delivery optics. (b) Five sample interferometer shots [open circles in (a)], separated in measured phase by $\sim\pi/2$ rad. All images are filtered with principal component analysis.

It can be challenging to measure small phase gradients with spatial frequencies $\kappa \ll 1/\sigma$, where σ is the width of the atom ensemble. In this limit, less than one fringe extends across the cloud, so the fringe fitting method in Fig. 2(b) cannot be used. Instead, the gradient can be estimated by measuring phase differences across the ensemble (e.g., with ellipse fits [24,29]), but this procedure can be sensitive to fluctuations in the atomic density distribution (width, position, and shape).

To circumvent these issues, we take advantage of PSR by applying an additional shear that augments the residual Coriolis shear Φ_C. An additional tilt of $\delta\theta = \pm 60\ \mu$rad about the x axis is added for the final interferometer pulse. This introduces a horizontal shear Φ_H with approximately 2.5 fringe periods across the cloud, enough to use fringe fitting to extract the spatial frequency. Subtracting off the known contribution of the additional tilt then yields a measurement of the small residual Coriolis shear. This technique of shifting a small phase gradient to a larger spatial frequency is analogous to a heterodyne measurement in the time domain. In both cases, the heterodyne process circumvents low frequency noise.

Depending on the sign of the tilt angle, the applied shear adds to or subtracts from Φ_C. The combined phase gradient is then $\kappa_\pm \equiv k_{\text{eff}}|\delta\theta|t_3/t_d \pm \kappa_{C,y}$. By alternating the sign of the additional 60 μrad tilt and subtracting the results, we realize a differential measurement whereby systematic uncertainty in the applied shear is mitigated: $\Delta\kappa \equiv \kappa_+ - \kappa_- = 2\kappa_{C,y}$, independent of $|\delta\theta|$.

Figure 4 shows the expected linear scaling of the differential spatial frequency $\Delta\kappa$ as a function of the applied rotation angle $\delta\phi_E$. A linear fit to the data yields a horizontal intercept that indicates the direction of true north with a precision of 10 mdeg. An apparatus optimized for

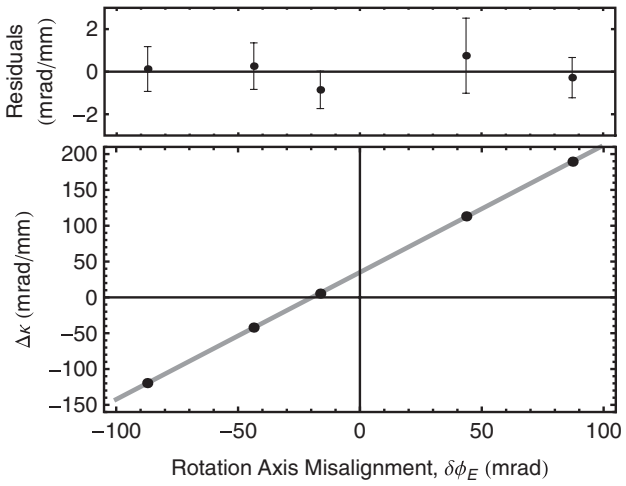

FIG. 4. Gyrocompass using PSR. Each $\Delta\kappa$ point is the combination of 40 trials, 20 each at two applied tilt values ($\delta\theta = \pm 60\ \mu$rad). The horizontal intercept of a linear fit gives the direction of true north.

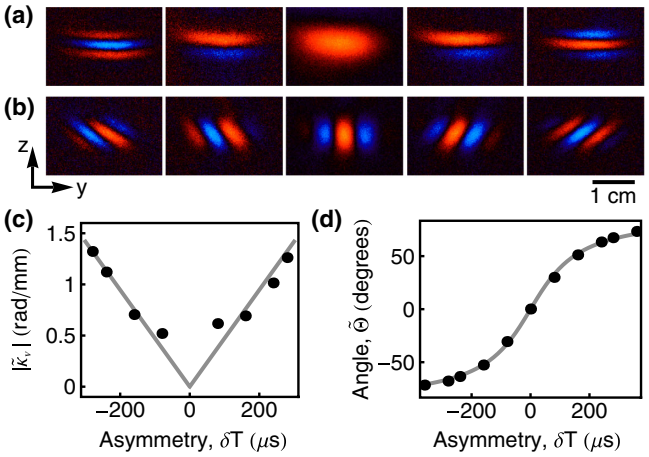

FIG. 5 (color online). Arbitrary control of spatial fringe direction. (a) Second-highest variance principal components from sets of 20 trials with timing asymmetry $\delta T = -240, -160, 0, +160, +240$ μs (left to right). (b) Comparable images for trials with both a beam tilt $\delta\theta = 40$ μrad and $\delta T = -160, -80, 0, +80, +160$ μs. (c) Measured fringe spatial frequency extracted from fits to principal component filtered images with vertical fringes. (d) Measured fringe angle extracted from fits to images with tilted fringes. In both (c) and (d), the curves are predictions with no free parameters.

gyrocompass performance could achieve similar or better precision in a more compact form factor. Also, this method does not require a vibrationally stable environment since the measurement uses the fringe period, not the overall phase.

Finally, we show how combining beam tilts and interferometer timing asymmetries provides arbitrary control over the spatial wave vector $\boldsymbol{\kappa}$ of the applied phase shear. While a beam tilt applies a shear transverse to the interferometer beam axis, timing asymmetry yields a shear parallel to the beam axis ($\boldsymbol{\kappa} \parallel \mathbf{k}_{\text{eff}}$) in the point source limit [16]. To create an asymmetric interferometer, we offset the central π pulse by $\delta T/2$ such that the time between the first and second pulses ($T + \delta T/2$) is different from the time between the second and third pulses ($T - \delta T/2$). The resulting phase shift $\Phi_V = k_{\text{eff}} v_z \delta T$ depends on the atoms' Doppler shift along the direction of $\mathbf{k}_{\text{eff}}$. The phase shear at detection is then $\kappa_V = \partial_z \Phi_V = k_{\text{eff}} \delta T / t_d$. Figure 5(a) shows the resulting vertical fringes, which are orthogonal to those from beam tilts [Fig. 2(a)] and are simultaneously visible on both CCD cameras. The fitted fringe frequency shown in Fig. 5(c) exhibits the expected linear dependence on δT, deviating at low spatial frequency due to the difficulty of fitting a fringe with $\kappa \sim 1/\sigma$.

For vertical fringes, the imaging pulse reduces the detected spatial frequency by stretching the cloud vertically. We independently characterize this stretch by measuring the fringe period as a function of imaging duration τ and extrapolating to $\tau = 0$. The results indicate a fractional stretch rate of $\alpha = 0.12$ ms^{-1}. The modified prediction for the spatial frequency is $\tilde{\kappa}_V = \kappa_V/(1 + \alpha\tau)$. With the $\tau = 2$ ms imaging time used, this agrees well with the measurements of Fig. 5(c) with no free parameters.

By combining beam-tilt shear κ_H with timing asymmetry shear κ_V, we can create spatial fringes at arbitrary angles. The composite shear is at angle $\Theta = \arctan(\kappa_V/\kappa_H) = \arctan[\delta T/(\delta\theta t_3)]$. Figures 5(b) and 5(d) show fringe images and extracted angles using a $\delta\theta = 40$ μrad beam tilt combined with a range of timing asymmetries. To find the angles, we apply Fourier and principal component filters and fit with a two-dimensional Gaussian envelope modulated by an interference term $P(\mathbf{r})$. We again correct for stretching during detection, which affects the measured angles. The modified prediction $\tilde{\Theta} = \text{arccot}[(1 + \alpha\tau)\cot\Theta]$ shows good agreement with the measured angles of Fig. 5(d) with no free parameters.

We have demonstrated a precision gyrocompass with PSR, but arbitrary control of the shear angle facilitates measurements of phase shifts and gradients from any origin. For example, a vertical gravity gradient T_{zz} induces a phase shear $k_{\text{eff}} T_{zz} v_z T^3$. This translates the measured angles of Fig. 5(d) such that $\Theta = \arctan[(\delta T - T_{zz} T^3)/(\delta\theta t_3)]$. For our parameters, this yields an effective asymmetry of 2 ns/E. PSR also enables measurements of nonlinear phase variations, including optical wavefront aberrations [24]. For precision measurements dependent on absolute phase (gravimetry, atomic recoil measurements, etc.), PSR can suppress systematic error by making phase measurements independent of drifts in the contrast envelope. Finally, we expect PSR to be enabling for future inertial sensors operating on dynamic platforms, where single-shot estimation of phase and contrast is vital.

The authors would like to thank Philippe Bouyer, Shengwey Chiow, Tim Kovachy, and Jan Rudolph for valuable discussions and contributions to the apparatus. A. S. acknowledges support from the NSF GRFP. S. M. D. acknowledges support from the Gerald J. Lieberman program. This work was supported in part by NASA GSFC Grant No. NNX11AM31A.

*kasevich@stanford.edu

[1] *Atom Interferometry*, edited by P. R. Berman (Academic, San Diego, 1997).
[2] J. B. Fixler, G. T. Foster, J. M. McGuirk, and M. A. Kasevich, Science **315**, 74 (2007).
[3] G. Lamporesi, A. Bertoldi, L. Cacciapuoti, M. Prevedelli, and G. M. Tino, Phys. Rev. Lett. **100**, 050801 (2008).
[4] R. Bouchendira, P. Cladé, S. Guellati-Khélifa, F. Nez, and F. Biraben, Phys. Rev. Lett. **106**, 080801 (2011).
[5] J. M. Hogan, D. M. S. Johnson, and M. A. Kasevich, in *Proceedings of the International School of Physics "Enrico Fermi,"*, edited by E. Arimondo, W. Ertmer, and W. P. Schleich (IOS Press, Amsterdam, 2009) p. 411.
[6] S. Dimopoulos, P. Graham, J. Hogan, and M. Kasevich, Phys. Rev. Lett. **98**, 111102 (2007).

[7] M. A. Hohensee, S. Chu, A. Peters, and H. Müller, Phys. Rev. Lett. **106**, 151102 (2011).
[8] S. Dimopoulos, P. W. Graham, J. M. Hogan, M. A. Kasevich, and S. Rajendran, Phys. Rev. D **78**, 122002 (2008).
[9] P. W. Graham, J. M. Hogan, M. A. Kasevich, and S. Rajendran, Phys. Rev. Lett. **110**, 171102 (2013).
[10] T. L. Gustavson, P. Bouyer, and M. A. Kasevich, Phys. Rev. Lett. **78**, 2046 (1997).
[11] R. Geiger, V. Ménoret, G. Stern, N. Zahzam, P. Cheinet, B. Battelier, A. Villing, F. Moron, M. Lours, Y. Bidel, A. Bresson, A. Landragin, and P. Bouyer, Nat. Commun. **2**, 474 (2011).
[12] A. Peters, K. Y. Chung, and S. Chu, Metrologia **38**, 25 (2001).
[13] J. M. McGuirk, G. T. Foster, J. B. Fixler, M. J. Snadden, and M. A. Kasevich, Phys. Rev. A **65**, 033608 (2002).
[14] M. Kasevich and S. Chu, Appl. Phys. B **54**, 321 (1992).
[15] M. Murty, Appl. Opt. **3**, 531 (1964).
[16] H. Müntinga *et al.*, Phys. Rev. Lett. **110**, 093602 (2013).
[17] T. Schumm, S. Hofferberth, L. M. Andersson, S. Wildermuth, S. Groth, I. Bar-Joseph, J. Schmiedmayer, and P. Krüger, Nat. Phys. **1**, 57 (2005).
[18] F. Baumgärtner, R. J. Sewell, S. Eriksson, I. Llorente-Garcia, J. Dingjan, J. P. Cotter, and E. A. Hinds, Phys. Rev. Lett. **105**, 243003 (2010).
[19] S. B. Cahn, A. Kumarakrishnan, U. Shim, T. Sleator, P. R. Berman, and B. Dubetsky, Phys. Rev. Lett. **79**, 784 (1997).
[20] S. Gupta, K. Dieckmann, Z. Hadzibabic, and D. Pritchard, Phys. Rev. Lett. **89**, 140401 (2002).
[21] S. Beattie, B. Barrett, M. Weel, I. Chan, C. Mok, S. B. Cahn, and A. Kumarakrishnan, Phys. Rev. A **77**, 013610 (2008).
[22] S. Wu, A. Tonyushkin, and M. G. Prentiss, Phys. Rev. Lett. **103**, 034101 (2009).
[23] B. Barrett, A. Carew, S. Beattie, and A. Kumarakrishnan, Phys. Rev. A **87**, 033626 (2013).
[24] S. M. Dickerson, J. M. Hogan, A. Sugarbaker, D. M. S. Johnson, and M. A. Kasevich, Phys. Rev. Lett. **111**, 083001 (2013).
[25] At this low density, atomic collisions are negligible.
[26] S. Dickerson, J. M. Hogan, D. M. S. Johnson, T. Kovachy, A. Sugarbaker, S.-w. Chiow, and M. A. Kasevich, Rev. Sci. Instrum. **83**, 065108 (2012).
[27] We spatially separate the output ports because the imaging procedure is not state selective.
[28] The point source limit is relevant here only as an imaging artifact, resulting from $t_d > t_3$. It is not necessary for beam-tilt PSR.
[29] G. T. Foster, J. B. Fixler, J. M. McGuirk, and M. A. Kasevich, Opt. Lett. **27**, 951 (2002).
[30] S. R. Segal, Q. Diot, E. A. Cornell, A. A. Zozulya, and D. Z. Anderson, Phys. Rev. A **81**, 053601 (2010).
[31] We determine this correction factor with an independent measurement of the fringe spatial frequency versus imaging time. For horizontal fringes, the observed spatial frequency decreases by 5% for 5 ms imaging.